

Tensile Instability in a Thick Elastic Body

Johannes T. B. Overvelde,^{1,2} David M. J. Dykstra,¹ Rijk de Rooij,¹ James Weaver,³ and Katia Bertoldi^{1,4,*}

¹John A. Paulson School of Engineering and Applied Sciences, Harvard University, Cambridge, Massachusetts 02138, USA

²FOM Institute AMOLF, Science Park 104, 1098 XG Amsterdam, Netherlands

³Wyss Institute for Biologically Inspired Engineering, Harvard University, Cambridge, Massachusetts 02138, USA

⁴Kavli Institute, Harvard University, Cambridge, Massachusetts 02138, USA

(Received 13 April 2016; revised manuscript received 1 July 2016; published 24 August 2016)

A range of instabilities can occur in soft bodies that undergo large deformation. While most of them arise under compressive forces, it has previously been shown analytically that a tensile instability can occur in an elastic block subjected to equitriaxial tension. Guided by this result, we conducted centimeter-scale experiments on thick elastomeric samples under generalized plane strain conditions and observed for the first time this elastic tensile instability. We found that equibiaxial stretching leads to the formation of a wavy pattern, as regions of the sample alternatively flatten and extend in the out-of-plane direction. Our work uncovers a new type of instability that can be triggered in elastic bodies, enlarging the design space for smart structures that harness instabilities to enhance their functionality.

DOI: 10.1103/PhysRevLett.117.094301

A variety of instabilities can be triggered when elastic structures are subjected to mechanical loadings [1,2]. While such instabilities have traditionally been considered as the onset of failure, a new trend is emerging in which the dramatic geometric changes induced by them are harnessed to enable new functionalities [3–6]. For example, buckling of thin beams and shells has been instrumental in the design of stretchable electronics [7,8], complex 3D architectures [9,10], materials with negative Poisson's ratio [11–13], and tunable acoustic metamaterials [14,15]. Moreover, changes in surface curvature due to wrinkling and creases have enabled the control of surface chemistry [16], wettability [17], adhesion [18,19], and drag [20].

While most elastic instabilities are the result of compressive forces, elastic bodies may also become unstable under tensile loading. For example, a wrinkling instability can be triggered in a thin elastic sheet under uniaxial extension [21–23], and a meniscus instability can occur when a thin layer of elastic material is confined and pulled in the out-of-plane direction resulting in a periodic array of fingers at its edges [24,25]. Moreover, it is well known that a cavity can undergo a sudden expansion upon reaching a critical internal pressure. This instability is not only observed in the case of thin membranes [26,27], but also persists in thick solid bodies where it is often referred to as cavitation [28]. Since cavitation is the only tensile instability that has been found in thick elastic bodies, a natural question to ask is whether other elastic tensile instabilities can occur in such systems.

About half a century ago, it was shown analytically that a tension instability can be triggered in a block of incompressible elastic material subjected to equitriaxial tension [Fig. 1(a)] [29–33]. More specifically, it has been demonstrated that when a cube with edges of length L and made

from an incompressible Neo-Hookean material with initial shear modulus μ is subjected to uniform tractions resulting in six tensile normal forces of magnitude F , two possible equilibrium solutions exist (see Supplemental Material: *Analytical exploration* [34]):

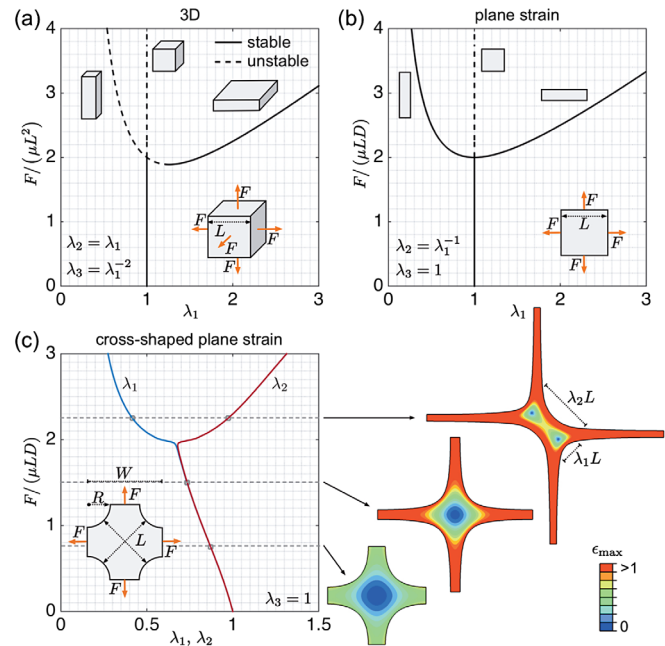


FIG. 1. Force-stretch bifurcation diagram for (a) a cube subjected to triaxial tension, (b) a square under plane strain conditions subjected to biaxial tension, and (c) a biaxially stretched cross-shaped sample under plane strain conditions. The solid and dashed lines represent stable and unstable load paths, respectively. The contours show the maximum in-plane principal strain. Note that (a) and (b) were obtained analytically, while (c) was obtained using finite element analysis.

$$\lambda_1 = \lambda_2 = \lambda_3 = 1 \quad (1)$$

and

$$\frac{F}{\mu L^2} = \lambda_1 + \frac{1}{\lambda_1^2}, \quad \lambda_2 = \lambda_1, \quad \lambda_3 = \lambda_1^{-2}, \quad (2)$$

λ_i being the principle stretches. As a result, when the applied force F is gradually increased, the block maintains its undeformed configuration ($\lambda_i = 1$) until $F = 2\mu L^2$. At this point, the solution bifurcates, the initial branch [Eq. (1)] becomes unstable, and the cube snaps to the second branch [Eq. (2)] and, therefore, suddenly flattens. It should be noted that this instability has only been demonstrated analytically and has not been triggered experimentally. In this Letter, guided by both analytical and finite element models, we report the first experimental observation of this instability in a thick elastomeric sample that is stretched equibiaxially under generalized plane strain conditions.

Designing an experiment to realize the tension instability.—Although it is possible to analytically obtain the triaxial tensile instability for a cube under triaxial tension, it is challenging to realize the same conditions in experiments. First, the instability requires the application of six equal and orthogonal forces to a block of material. Second, the forces need to be evenly spread across the whole surface, and third, the boundary conditions have to adapt to the large deformation after the instability has occurred.

In an effort to simplify the boundary conditions, we start by considering an incompressible elastomeric block under plane strain conditions (i.e., $\lambda_3 = 1$ and $\lambda_2 = \lambda_1^{-1}$) subjected to four in-plane tensile forces of magnitude F as indicated in Fig. 1(b). When assuming a Neo-Hookean material, the potential energy of the system Π is given by

$$\Pi = \frac{\mu L^2 D}{2} \left(\lambda_1^2 + \frac{1}{\lambda_1^2} - 2 \right) - FL \left(\lambda_1 + \frac{1}{\lambda_1} - 2 \right), \quad (3)$$

in which D is the out-of-plane thickness of the sample. The equilibrium solutions are then found by minimizing Π (i.e., $\partial\Pi/\partial\lambda_1 = 0$), yielding

$$\lambda_1 = \lambda_2 = \lambda_3 = 1 \quad (4)$$

and

$$\frac{F}{\mu LD} = \lambda_1 + \frac{1}{\lambda_1}, \quad \lambda_2 = \lambda_1^{-1}, \quad \lambda_3 = 1, \quad (5)$$

which are stable only if

$$\frac{\partial^2 \Pi}{\partial \lambda^2} = \mu L^2 D \left(1 + \frac{3}{\lambda_1^4} \right) - FL \left(\frac{2}{\lambda_1^3} \right) > 0. \quad (6)$$

Interestingly, the solutions defined by Eqs. (4) and (5) are similar to those found for the triaxial case [Eqs. (1) and (2)] and still show a bifurcation point at $F = 2\mu LD$. Differently, for the plane strain case, no snap-through instability is observed since the force monotonically increases, as indicated in Fig. 1(b). Note that during loading the out-of-plane tensile stress that builds up in the material due to the plane strain conditions plays an important role, since no instability occurs if we assume plane stress conditions (see Supplemental Material: *Analytical exploration* [34]).

Next, to apply uniformly distributed traction forces to the edges of the square, we consider a cross-shaped specimen, as typically done for biaxial experiments [37,38]. More specifically, we consider a square of edges W with circles of radius $R = 0.31W$ cut from the corners. When assuming plane strain conditions, and applying an outward displacement to the straight boundaries of the sample, we expect its center to undergo a triaxial state of stress. To compare the response of the cross-shaped sample with our analytical predictions for a square [Fig. 1(b)], we monitor the evolution of the two diagonals with initial length $L = \sqrt{2}W - 2R$ located at the center of the sample, as shown in Fig. 1(c), and introduce the stretches λ_1 and λ_2 to define their deformation.

Next, to determine the response of the cross-shaped sample upon loading, we performed 2D implicit finite element analysis under plane strain conditions using Abaqus (Dassault Systèmes). We captured the material response using a nearly incompressible Neo-Hookean model characterized by a ratio between the bulk modulus K and shear modulus μ of $K/\mu = 20$ [39]. The four straight edges of the samples were loaded by a force F in their normal direction, while allowing movement in the orthogonal direction. Moreover, to break the symmetry of the structure, we introduced a small imperfection by increasing the radius of two diagonally placed holes by 0.2%.

The results of our simulations are shown in Fig. 1(c), where we report the evolution of λ_1 and λ_2 as a function of the normalized force $F/(\mu LD)$. We find that an instability is triggered at $F/(\mu LD) \approx 2$, resulting in a sudden flattening of the central part of the sample similar to that predicted by the analytical model. However, different from the analytical results shown in Fig. 1(b), our results reveal that prior to the instability the central domain slightly reduces in size (i.e., $\lambda_1 = \lambda_2 \neq 1$). This discrepancy arises because the deformation in the numerical model is not homogeneous, as assumed in the analytical model [see distribution of the maximum in-plane strain ϵ_{\max} in Fig. 1(c)].

Experimental result.—Having demonstrated numerically that an elastic instability is triggered when a cross-shaped sample under plane strain conditions is subjected to biaxial tension, we fabricated a thick sample from a silicon rubber (Ecoflex 0030, Smooth-On) with a shear modulus $\mu = 0.0216$ MPa [Fig. 2(a) and Supplemental Material: *Experiments* [34]]. To constrain the out-of-plane deformation we connected each side of the sample to a stiffer silicon

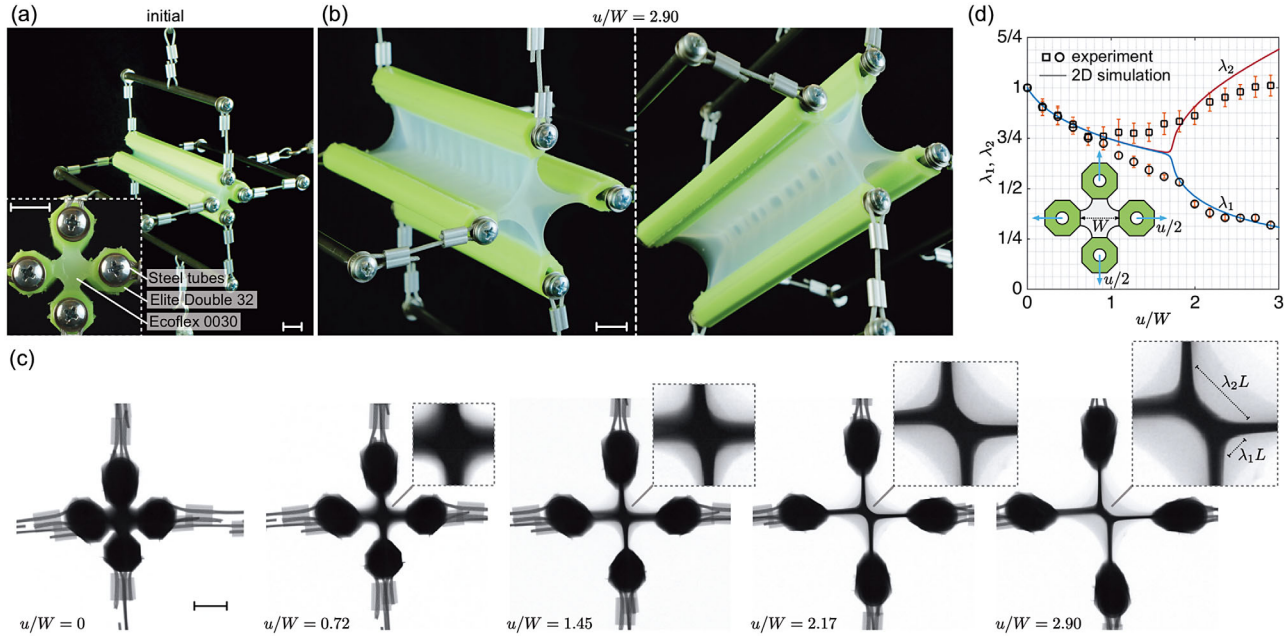


FIG. 2. (a) Experimental setup to subject our thick cross-shaped sample to biaxial tension. (b) Top and bottom views of the deformed sample at $u/W = 2.90$. (c) Cross-sectional views of the sample at $u/W = 0, 0.72, 1.45, 2.17$, and 2.90 obtained using a micro-CT (computed tomography) x-ray imaging machine. (d) Relation between the normalized displacement u/W applied to the sample and the stretches λ_1 and λ_2 of the diagonals located at the center of the sample. The results were obtained by manually processing the images and averaging five individual measurements (the error bars indicate the standard deviation) (scale bars 10 mm).

elastomer (Elite Double 32, Zhermack) characterized by $\mu = 0.262$ MPa [40]. Moreover, to approximate the plane strain conditions assumed in our calculations, we took $D/W \gg 1$ ($D = 132$ mm and $W = 14$ mm). Finally, we placed steel tubes inside the stiffer elastomer to connect it through cables to a rigid frame that was used to stretch the sample. Figure 2(b) shows the observed deformation at $u/W = 2.9$, $u/2$ being the displacement applied to each straight edge. Since boundary effects prevented us from clearly observing the instability (Fig. S6 in Supplemental Material [34]), we acquired x-ray transmission images at different levels of applied deformation [Fig. 2(c) herein and Movie 1 in Supplemental Material [34]]. We then manually processed the images to obtain the stretches, λ_1 and λ_2 , that define the deformation of the diagonals of the central domain, exactly as in our simulations. The results reported in Fig. 2(d) indicate that at $u/W \approx 1$ an instability is triggered that breaks the symmetry and initiates a flattening of the center of the sample. While the experimental results agree relatively well with the 2D plane strain simulations, we find that the instability is triggered for smaller deformations. This discrepancy is likely due to imperfections introduced during fabrication and loading, which tend to smoothen the sudden transition arising from the instability and result in an earlier flattening (Fig. S7 in Supplemental Material [34]).

Wavy pattern along the depth.—From the experiments we find that the instability not only results in the flattening of the center of the sample as predicted by the plane strain

simulations, but also introduces waves on the surfaces along the depth [Fig. 2(b)]. To better understand the formation of this wavy pattern, we conducted 3D explicit quasistatic finite element analysis and simulated the cross-shaped sample as used in the experiments; i.e., we modeled both the two elastomeric materials and steel tubes to exactly mimic the experimental conditions [41].

As shown in Fig. 3(a) herein and Movie 2 in Supplemental Material [34], our 3D simulations confirm the experimental observations. By monitoring the stretch of the diagonals defining the center region of the sample (along the depth), it becomes clear that the wavy pattern emerges the moment the sample becomes unstable at $u/W \approx 2$ [Fig. 3(b)]. In fact, for $u/W \lesssim 2$, λ_1 and λ_2 are constant along the depth of the sample, while for $u/W \gtrsim 2$, they oscillate periodically. Moreover, we also find that after the instability has occurred, the sample not only deforms nonuniformly in plane, but also in the out-of-plane direction. To highlight this point, in Fig. 3(c) we report the out-of-plane stretch λ_3 measured along the center line of the sample at different levels of applied loading. The results indicate that for $u/W \gtrsim 2$ there is an alternation between regions experiencing out-of-plane extension and compression along the depth of the sample.

Informed by the numerical results of Figs. 3(a)–3(c), we next extend our analytical model and assume that the elastic block consists of two layers, a and b , which can deform separately. We then impose generalized plane strain conditions

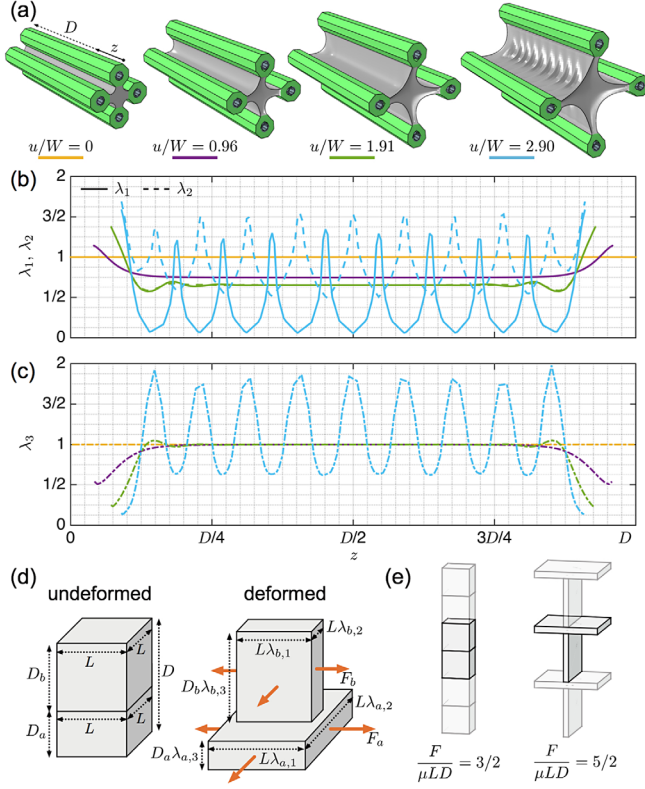


FIG. 3. (a) Numerical snapshots of the sample, (b) stretches that define the deformation of the diagonals of the central domain (λ_1 and λ_2) along the depth of the sample, and (c) out-of-plane stretch of the center line (λ_3) along the depth of the sample, at $u/W = 0, 0.96, 1.91, 2.90$. (d) Schematic of the bilayer under generalized plane strain conditions used in our analytical model. (e) Deformed states of the analytical model at $F/(\mu LD) = 3/2$ and $5/2$ for $D = 2L$.

$$\bar{h}\lambda_{a,3} + (1 - \bar{h})\lambda_{b,3} = 1, \quad (7)$$

where the stretches $\lambda_{a,3}$ and $\lambda_{b,3}$ are indicated in Fig. 3(d), and $\bar{h} = D_a/(D_a + D_b)$ sets the ratio between the depth of layer a and b in the undeformed configuration. If we further assume that the four in-plane forces applied to each layer depend on the initial size of the layer [i.e., $F_a = F\bar{h}$ and $F_b = F(1 - \bar{h})$, F being the total force applied to the two blocks], the potential energy takes the form (Supplemental Material: Analytical exploration [34])

$$\begin{aligned} \Pi = & \frac{\bar{h}\mu L^2 D}{2} \left(\lambda_{a,1}^2 + \frac{1}{\lambda_{a,1}^2 \lambda_{a,3}^2} + \lambda_{a,3}^2 - 3 \right) \\ & + \mu L^2 D \frac{1 - \bar{h}}{2} \left(\lambda_{b,1}^2 + \frac{(1 - \bar{h})^2}{\lambda_{b,1}^2 (1 - \bar{h}\lambda_{a,3})^2} \right. \\ & + \left. \frac{(1 - \bar{h}\lambda_{a,3})^2}{(1 - \bar{h})^2} - 3 \right) - F_a L \left(\lambda_{a,1} + \frac{1}{\lambda_{a,1} \lambda_{a,3}} - 2 \right) \\ & - F_b L \left(\lambda_{b,1} + \frac{1 - \bar{h}}{\lambda_{b,1} (1 - \bar{h}\lambda_{a,3})} - 2 \right), \end{aligned} \quad (8)$$

where $D = D_a + D_b$. Minimizing the energy results again in two possible solutions:

$$\lambda_{a,1} = 1 \quad \text{with} \quad 0 \leq \bar{h} \leq 1, \quad (9)$$

$$\frac{F}{\mu LD} = \lambda_{a,1} + \frac{1}{\lambda_{a,1}^2} \quad \text{with} \quad \bar{h} = \frac{\lambda_{a,1}^2 - 1}{\lambda_{a,1}^3 - 1}, \quad (10)$$

in which $\lambda_{a,3} = \lambda_{b,1} = \lambda_{b,2} = \lambda_{a,1}$ and $\lambda_{a,2} = \lambda_{b,3} = \lambda_{a,1}^{-2}$. We find that the solutions defined by Eqs. (9) and (10) are identical to those found for a cube subjected to equitriaxial tension [Eqs. (1) and (2)], and that a bifurcation occurs at $F/(\mu LD) = 2$. For $F/(\mu LD) < 2$ the system does not deform [as illustrated in Fig. 3(e) for $F/(\mu LD) = 3/2$], while for $F/(\mu LD) > 2$ one of the layers extends and the other flattens in the out-of-plane direction [as illustrated in Fig. 3(e) for $F/(\mu LD) = 5/2$], resulting in a wavy pattern that resembles the deformation shown in Figs. 2(b) and 3(a).

Outlook.—In this work, we experimentally showed that an instability can be triggered in a thick elastic body subjected to in-plane tensile forces and generalized plane strain conditions. While an instability was already analytically predicted in 1948 for a cube subjected to triaxial tension [29], here we extended the analysis to a configuration that can be tested experimentally, and found that the modified conditions result in a wavy pattern, as portions of the sample alternatively extend and flatten in the out-of-plane direction.

It should be noted that tensile loading conditions can also lead to cavitation in solids [28,42]. More specifically, for an incompressible Neo-Hookean material subjected to equitriaxial tension, it can be analytically derived that cavitation initiates at a pressure of $p_{\text{cav}} = 5\mu/2$ [43]. As a result, for the elastomeric cube of Fig. 1(a) subjected to triaxial tension, cavitation initiates at $F_{\text{cav}} = 5\mu L^2/2$. Although this critical value is 25% higher than that needed to flatten

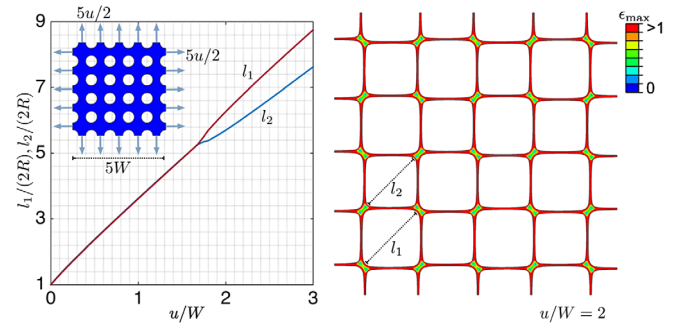


FIG. 4. Deformation of a mechanical metamaterial comprising a square array of circular pores subjected to equibiaxial tension. Similar to the case of the cross-shaped sample shown in Fig. 1(c), an instability is triggered at $u/W \approx 2$ resulting in a checkerboard pattern of pores with two different sizes. The contours represent the maximum in-plane strain ϵ_{max} .

the cube, we expect our sample to experience such a value of stress in the postbuckling regime. In fact, upon increasing the stretch applied to the sample to $u/W = 3.26$, we immediately see some cavities forming, which slowly increase in size when the applied deformation is maintained for a few hours (Movie 3 in Supplemental Material [34]).

Finally, the cross-shaped samples used in our experiments can be used to build a mechanical metamaterial by arranging them on a square lattice as shown in Fig. 4. By stretching the metamaterial biaxially (under plane strain conditions), an instability is triggered at $u/W \approx 2$ resulting in a checkerboard pattern of pores with two different sizes, as indicated by the evolution of the characteristic pore sizes l_1 and l_2 shown in Fig. 4. While the formation of this pattern has previously been observed in simulations of similar periodic porous structures [44–46], with the current work we have deciphered the underlying mechanism that leads to the instability. As such, we expect our study to open new avenues for the design of soft structures that harness instabilities for improved functionality.

This work was supported by the Materials Research Science and Engineering Center under NSF Grant No. DMR-1420570. K. B. also acknowledges support from the National Science Foundation (CMMI-1149456-CAREER). We thank Samuel Shian for his initial help with the experimental setup and Sahab Babaee and John Hutchinson for fruitful discussions.

*bertoldi@seas.harvard.edu

- [1] Z. Bažant and L. Cedolin, *Stability of Structures: Elastic, Inelastic, Fracture and Damage Theories* (World Scientific, Singapore, 2010).
- [2] Q. Wang and X. Zhao, *MRS Bull.* **41**, 115 (2016).
- [3] S. Singamaneni and V. V. Tsukruk, *Soft Matter* **6**, 5681 (2010).
- [4] D. Chen, J. Yoon, D. Chandra, A. J. Crosby, and R. C. Hayward, *J. Polym. Sci. B* **52**, 1441 (2014).
- [5] B. Florijn, C. Coulaiss, and M. van Hecke, *Phys. Rev. Lett.* **113**, 175503 (2014).
- [6] S. Cai, D. Breid, A. Crosby, Z. Suo, and J. Hutchinson, *J. Mech. Phys. Solids* **59**, 1094 (2011).
- [7] J. A. Rogers, T. Someya, and Y. Huang, *Science* **327**, 1603 (2010).
- [8] Y. Wang, R. Yang, Z. Shi, L. Zhang, D. Shi, E. Wang, and G. Zhang, *ACS Nano* **5**, 3645 (2011).
- [9] J. Kim, J. A. Hanna, M. Byun, C. D. Santangelo, and R. C. Hayward, *Science* **335**, 1201 (2012).
- [10] S. Xu, Z. Yan, K.-I. Jang, W. Huang, H. Fu, J. Kim, Z. Wei, M. Flavin, J. McCracken, R. Wang *et al.*, *Science* **347**, 154 (2015).
- [11] K. Bertoldi, P. M. Reis, S. Willshaw, and T. Mullin, *Adv. Mater.* **22**, 361 (2010).
- [12] J. T. B. Overvelde, S. Shan, and K. Bertoldi, *Adv. Mater.* **24**, 2337 (2012).
- [13] S. Babaee, J. Shim, J. C. Weaver, E. R. Chen, N. Patel, and K. Bertoldi, *Adv. Mater.* **25**, 5044 (2013).
- [14] K. Bertoldi and M. C. Boyce, *Phys. Rev. B* **77**, 052105 (2008).
- [15] P. Wang, F. Casadei, S. Shan, J. C. Weaver, and K. Bertoldi, *Phys. Rev. Lett.* **113**, 014301 (2014).
- [16] J. Kim, J. Yoon, and R. C. Hayward, *Nat. Mater.* **9**, 159 (2010).
- [17] P.-C. Lin and S. Yang, *Soft Matter* **5**, 1011 (2009).
- [18] P.-C. Lin, S. Vajpayee, A. Jagota, C.-Y. Hui, and S. Yang, *Soft Matter* **4**, 1830 (2008).
- [19] E. Chan, E. Smith, R. Hayward, and A. Crosby, *Adv. Mater.* **20**, 711 (2008).
- [20] D. Terwagne, M. Brojan, and P. M. Reis, *Adv. Mater.* **26**, 6608 (2014).
- [21] E. Cerda and L. Mahadevan, *Phys. Rev. Lett.* **90**, 074302 (2003).
- [22] B. Davidovitch, R. D. Schroll, D. Vella, M. Adda-Bedia, and E. A. Cerda, *Proc. Natl. Acad. Sci. U.S.A.* **108**, 18227 (2011).
- [23] H. Vandeparre, S. Gabriele, F. Brau, C. Gay, K. K. Parker, and P. Damman, *Soft Matter* **6**, 5751 (2010).
- [24] K. R. Shull, C. M. Flanagan, and A. J. Crosby, *Phys. Rev. Lett.* **84**, 3057 (2000).
- [25] J. S. Biggins, B. Saintyves, Z. Wei, E. Bouchaud, and L. Mahadevan, *Proc. Natl. Acad. Sci. U.S.A.* **110**, 12545 (2013).
- [26] D. R. Merritt and F. Weinhaus, *Am. J. Phys.* **46**, 976 (1978).
- [27] J. T. B. Overvelde, T. Kloek, J. J. A. D'haen, and K. Bertoldi, *Proc. Natl. Acad. Sci. U.S.A.* **112**, 10863 (2015).
- [28] A. N. Gent and P. B. Lindley, *Proc. R. Soc. A* **249**, 195 (1959).
- [29] R. S. Rivlin, *Phil. Trans. R. Soc. A* **240**, 491 (1948).
- [30] R. Hill, *J. Mech. Phys. Solids* **5**, 229 (1957).
- [31] M. F. Beatty, *Int. J. Solids Struct.* **3**, 23 (1967).
- [32] R. S. Rivlin, *Collected Papers of R. S. Rivlin: Volume I and II* (Springer, New York, 1997), pp. 398–404.
- [33] J. M. Ball and D. G. Schaeffer, *Math. Proc. Cambridge Philos. Soc.* **94**, 315 (1983).
- [34] See Supplemental Material at <http://link.aps.org/supplemental/10.1103/PhysRevLett.117.094301>, which includes Refs. [29–33, 35, 36], for supporting movies and an analytical exploration (describing a cube subjected to equitriaxial tension, a square under plane strain and plane stress conditions subjected to equibiaxial tension, and a block under generalized plane strain conditions subjected to equibiaxial tension), a numerical study looking at the effect of the material compressibility, and a description of the experiments (fabrication and testing).
- [35] R. Ogden, *Non-Linear Elastic Deformations* (Dover, New York, 1988).
- [36] M. C. Boyce and E. M. Arruda, *Rubber Chem. Technol.* **73**, 504 (2000).
- [37] E. Shiratori and K. Ikegami, *J. Mech. Phys. Solids* **16**, 373 (1968).
- [38] Y. Lecieux and R. Bouzidi, *Int. J. Solids Struct.* **47**, 2459 (2010).
- [39] The models were discretized using approximately 1.5×10^4 triangular quadratic elements (Abaqus element code CPE6). For the nearly incompressible Neo-Hookean model we

chose $K/\mu = 20$, as it provides a good balance between simulation time and accuracy (Supplemental Material: *Effect of material compressibility* [34]).

- [40] J. Shim, C. Perdigou, E. R. Chen, K. Bertoldi, and P. M. Reis, *Proc. Natl. Acad. Sci. U.S.A.* **109**, 5978 (2012).
- [41] We modeled the Elite Double 32 and Ecoflex 0030 using a nearly incompressible Neo-Hookean material model with $K/\mu = 20$. Moreover, we assumed that the steel tubes do not deform, and used approximately 5×10^5 linear elements to construct the model (Abaqus element code C3D6R and C3D8R). We further assumed that the bonding region between the two elastomers is infinitesimally thin and can be neglected. Note that since we used explicit analysis, we did not apply any imperfections.
- [42] J. M. Ball, *Phil. Trans. R. Soc. A* **306**, 557 (1982).
- [43] A. Gent, *Int. J. Nonlinear Mech.* **40**, 165 (2005).
- [44] K. Bertoldi and M. C. Boyce, *Phys. Rev. B* **78**, 184107 (2008).
- [45] J. T. Overvelde and K. Bertoldi, *J. Mech. Phys. Solids* **64**, 351 (2014).
- [46] J. Michel, O. Lopez-Pamies, P. P. Castañeda, and N. Triantafyllidis, *J. Mech. Phys. Solids* **55**, 900 (2007).

Supplemental Material

ANALYTICAL EXPLORATION

To identify the key components in the design of an elastic body that undergoes an instability when subjected to tensile forces, we analytically explore the equilibrium states of (i) an elastomeric cube subjected to equitriaxial tension, (ii) an elastomeric square under plane stress conditions subjected to equibiaxial tension, (iii) an elastomeric square under plane strain conditions subjected to equibiaxial tension and (iv) an elastomeric block under generalized plane strain conditions subjected to equibiaxial tension.

In all our calculations, we assume the elastic body to be made of an incompressible Neo-Hookean material, whose strain energy density function, W , is given by [1]

$$W = \frac{\mu}{2} (\lambda_1^2 + \lambda_2^2 + \lambda_3^2 - 3), \quad (\text{S1})$$

where μ is the initial shear modulus of the material and λ_i are the principal stretches, which are subjected to the incompressibility constraint $\lambda_1 \lambda_2 \lambda_3 = 1$.

Cube subjected to equitriaxial tension

Similar to previous studies [2–6], we consider a cube with sides of length L subjected to six orthogonal outward pointing forces as indicated in Fig. 1(a). Assuming that the cube undergoes a homogeneous deformation, its internal energy, U , equals

$$U = L^3 W = \frac{\mu L^3}{2} (\lambda_1^2 + \lambda_2^2 + \lambda_3^2 - 3), \quad (\text{S2})$$

and the work done by the external forces, V , is given by

$$\begin{aligned} V &= FL(\lambda_1 - 1) + FL(\lambda_2 - 1) + FL(\lambda_3 - 1) \\ &= FL(\lambda_1 + \lambda_2 + \lambda_3 - 3). \end{aligned} \quad (\text{S3})$$

It follows that the potential energy for the system, $\Pi = U - V$, is given by

$$\Pi = \frac{\mu L^3}{2} \left(\lambda_1^2 + \lambda_2^2 + \frac{1}{\lambda_1^2 \lambda_2^2} - 3 \right) - FL \left(\lambda_1 + \lambda_2 + \frac{1}{\lambda_1 \lambda_2} - 3 \right), \quad (\text{S4})$$

where we have used the fact that $\lambda_3 = 1/(\lambda_1 \lambda_2)$ due to incompressibility of the material. The equilibrium solutions can then be found by minimizing Π with respect to λ_1 and λ_2 ,

$$\frac{\partial \Pi}{\partial \lambda_1} = \mu L^3 \left(\lambda_1 - \frac{1}{\lambda_1^3 \lambda_2^2} \right) - FL \left(1 - \frac{1}{\lambda_1^2 \lambda_2} \right) = 0, \quad (\text{S5})$$

$$\frac{\partial \Pi}{\partial \lambda_2} = \mu L^3 \left(\lambda_2 - \frac{1}{\lambda_1^2 \lambda_2^3} \right) - FL \left(1 - \frac{1}{\lambda_1 \lambda_2^2} \right) = 0. \quad (\text{S6})$$

Interestingly, there are two distinct solutions that satisfy Eqs. (S5) and (S6),

$$\lambda_1 = \lambda_2 = \lambda_3 = 1, \quad (\text{S7})$$

and

$$\frac{F}{\mu L^2} = \lambda_1 + \frac{1}{\lambda_1^2}, \quad \lambda_2 = \lambda_1, \quad \lambda_3 = \lambda_1^{-2}. \quad (\text{S8})$$

Moreover, note that the two solutions defined by Eqs. (S7)-(S8) are stable when the Hessian of the potential energy, H , is positive definite. This requires that

$$\frac{\partial^2 \Pi}{\partial \lambda_1^2} > 0, \quad \text{and} \quad \frac{\partial^2 \Pi}{\partial \lambda_1^2} \frac{\partial^2 \Pi}{\partial \lambda_2^2} - \frac{\partial^2 \Pi}{\partial \lambda_1 \partial \lambda_2} \frac{\partial^2 \Pi}{\partial \lambda_2 \partial \lambda_1} > 0, \quad (\text{S9})$$

in which

$$\frac{\partial^2 \Pi}{\partial \lambda_1^2} = \mu L^3 \left(1 + \frac{3}{\lambda_1^4 \lambda_2^2} \right) - FL \left(\frac{2}{\lambda_1^3 \lambda_2} \right) \quad (\text{S10})$$

$$\frac{\partial^2 \Pi}{\partial \lambda_1 \partial \lambda_2} = \frac{\partial^2 \Pi}{\partial \lambda_2 \partial \lambda_1} = \frac{2\mu L^3}{\lambda_1^3 \lambda_2^3} - \frac{FL}{\lambda_1^2 \lambda_2^2} \quad (\text{S11})$$

$$\frac{\partial^2 \Pi}{\partial \lambda_2^2} = \mu L^3 \left(1 + \frac{3}{\lambda_1^2 \lambda_2^4} \right) - FL \left(\frac{1}{\lambda_1 \lambda_2^3} \right). \quad (\text{S12})$$

As a result, when the applied force F is gradually increased, the block maintains its undeformed configuration ($\lambda_i = 1$) until $F = 2\mu L^2$. At this point, the solution bifurcates, the initial branch (Eq. (S7)) becomes unstable and the cube snaps to the second branch (Eq. (S8)) and therefore suddenly flattens (see Fig. 1(a)).

Square under plane stress conditions subjected to equibiaxial tension

We next show that no instability occurs when an elastomeric square under plane stress conditions is subjected to equibiaxial tension. Since in this case no work is done in the out-of-plane direction, the work done by the applied forces reduces to

$$V = FL (\lambda_1 + \lambda_2 - 2), \quad (\text{S13})$$

so that the potential energy for the system becomes

$$\Pi = \frac{\mu L^2 D}{2} \left(\lambda_1^2 + \lambda_2^2 + \frac{1}{\lambda_1^2 \lambda_2^2} - 3 \right) - FL (\lambda_1 + \lambda_2 - 2), \quad (\text{S14})$$

where D is the depth of the sample, and we have used the incompressibility condition (i.e. $\lambda_1 \lambda_2 \lambda_3 = 1$). Equilibrium requires that

$$\frac{\partial \Pi}{\partial \lambda_1} = \mu L^2 D \left(\lambda_1 - \frac{1}{\lambda_1^3 \lambda_2^2} \right) - FL = 0, \quad (\text{S15})$$

$$\frac{\partial \Pi}{\partial \lambda_2} = \mu L^2 D \left(\lambda_2 - \frac{1}{\lambda_1^2 \lambda_2^3} \right) - FL = 0, \quad (\text{S16})$$

that are only satisfied for

$$\frac{F}{\mu L D} = \left(\lambda_1 - \frac{1}{\lambda_1^5} \right), \quad \lambda_2 = \lambda_1, \quad \lambda_3 = \lambda_1^{-2}. \quad (\text{S17})$$

Note that this solution is always stable.

Square under plane strain conditions subjected to equibiaxial tension

Differently from the plane stress case, an instability can be observed when an elastomeric square under plane strain conditions is subjected to equibiaxial tension. Since for plane strain $\lambda_3 = 1$, the incompressibility constraint reduces to $\lambda_1 = \lambda_2^{-1}$. It follows that the potential energy for the system is given by

$$\Pi = \frac{\mu L^2 D}{2} \left(\lambda_1^2 + \frac{1}{\lambda_1^2} - 2 \right) - FL \left(\lambda_1 + \frac{1}{\lambda_1} - 2 \right), \quad (\text{S18})$$

so that the equilibrium configurations are found by setting

$$\frac{d\Pi}{d\lambda_1} = \mu L^2 D \left(\lambda_1 - \frac{1}{\lambda_1^3} \right) - FL \left(1 - \frac{1}{\lambda_1^2} \right) = 0. \quad (\text{S19})$$

Interestingly, there are two distinct solutions that satisfy Eq. (S19),

$$\lambda_1 = \lambda_2 = \lambda_3 = 1, \quad (\text{S20})$$

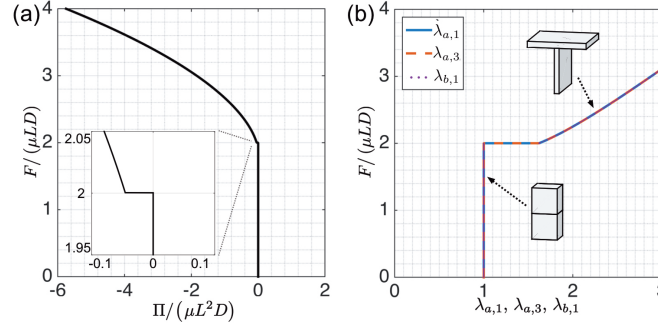


FIG. S1: Incremental solution obtained with the *fmincon* function in Matlab for the general plane strain case. (a) Relation between the normalized force $F/(\mu LD)$ and the potential energy $\Pi/(\mu L^2 D)$. (b) Relation between the normalized force $F/(\mu LD)$ and the characteristic stretches $\lambda_{a,1}$, $\lambda_{a,3}$ and $\lambda_{b,1}$.

and

$$\frac{F}{\mu LD} = \lambda_1 + \frac{1}{\lambda_1}, \quad \lambda_2 = \lambda_1^{-1}, \quad \lambda_3 = 1. \quad (\text{S21})$$

Furthermore, stability requires

$$\frac{\partial^2 \Pi}{\partial \lambda_1^2} = \mu L^2 D \left(1 + \frac{3}{\lambda_1^4} \right) - FL \left(\frac{2}{\lambda_1^3} \right) > 0. \quad (\text{S22})$$

It should be noted that the solutions defined by Eqs. (S20)-(S21) are similar to those found for the triaxial case (Eqs. (S7)-(S8)) and still show a bifurcation point at $F = 2\mu LD$. Differently, for the plane strain case no snap-through instability is observed since the force monotonically increases, as indicated in Fig. 1(b).

Block under generalized plane strain conditions subjected to equibiaxial tension

Our experimental and 3D numerical results indicate that the instability not only results in the flattening of the center of the sample as predicted by the plane strain simulations, but also introduces waves on the surfaces along the depth. Informed by these results, we extend our analytical model and assume that the elastic block consists of two layers, a and b , which deform separately and homogeneously (Fig. 3(d)). The deformation of the system is then fully described by six stretches, $\lambda_{a,i}$ for layer a and $\lambda_{b,i}$ for layer b ($i = 1, 2, 3$), subjected to the incompressibility constraints

$$\lambda_{a,1} \lambda_{a,2} \lambda_{a,3} = 1, \quad (\text{S23})$$

$$\lambda_{b,1} \lambda_{b,2} \lambda_{b,3} = 1. \quad (\text{S24})$$

Next, we impose generalized plane strain conditions, so that

$$D_a \lambda_{a,3} + D_b \lambda_{b,3} = D_a + D_b = D, \quad (\text{S25})$$

which can be rewritten as

$$\bar{h} \lambda_{a,3} + (1 - \bar{h}) \lambda_{b,3} = 1, \quad (\text{S26})$$

where $\bar{h} = D_a/(D_a + D_b)$ sets the ratio between the depth of layer a and b in the undeformed configuration.

Furthermore, given the dimensions and forces indicated in Fig. 3(d), the potential energy for layers a and b is given by

$$U_a = \frac{\mu L^2 D_a}{2} (\lambda_{a,1}^2 + \lambda_{a,2}^2 + \lambda_{a,3}^2 - 3), \quad (\text{S27})$$

$$U_b = \frac{\mu L^2 D_b}{2} (\lambda_{b,1}^2 + \lambda_{b,2}^2 + \lambda_{b,3}^2 - 3), \quad (\text{S28})$$

while the work done by the applied forces equals

$$V_a = F_a L (\lambda_{a,1} + \lambda_{a,2} - 2), \quad (\text{S29})$$

$$V_b = F_b L (\lambda_{b,1} + \lambda_{b,2} - 2). \quad (\text{S30})$$

By further assuming that the four in-plane forces applied to each layer depend on the initial size of the layer (i.e. $F_a = F\bar{h}$ and $F_b = F(1 - \bar{h})$, F being the total force applied to the two blocks) and using the conditions from Eqs. (S23)-(S26), Eqs. (S27)-(S30) can be rewritten as

$$U_a = \frac{\mu\bar{h}DL^2}{2} \left(\lambda_{a,1}^2 + \frac{1}{\lambda_{a,1}^2\lambda_{a,3}^2} + \lambda_{a,3}^2 - 3 \right), \quad (\text{S31})$$

$$U_b = \frac{\mu(1 - \bar{h})DL^2}{2} \left(\lambda_{b,1}^2 + \frac{(1 - \bar{h})^2}{\lambda_{b,1}^2(1 - \bar{h}\lambda_{a,3})^2} + \frac{(1 - \bar{h}\lambda_{a,3})^2}{(1 - \bar{h})^2} - 3 \right), \quad (\text{S32})$$

$$V_a = F\bar{h}L \left(\lambda_{a,1} + \frac{1}{\lambda_{a,1}\lambda_{a,3}} - 2 \right), \quad (\text{S33})$$

$$V_b = F(1 - \bar{h})L \left(\lambda_{b,1} + \frac{1 - \bar{h}}{\lambda_{b,1}(1 - \bar{h}\lambda_{a,3})} - 2 \right), \quad (\text{S34})$$

in which the independent variables have been reduced to $\lambda_{a,1}$, $\lambda_{a,3}$, $\lambda_{b,1}$ and \bar{h} . Finally, the potential energy for the system can be obtained as

$$\Pi = U_a + U_b - V_a - V_b. \quad (\text{S35})$$

and the stable equilibrium solutions can be determined by minimizing the potential energy Π ,

$$\frac{\partial \Pi}{\partial \lambda_{a,1}} = 0, \quad \frac{\partial \Pi}{\partial \lambda_{a,3}} = 0, \quad \frac{\partial \Pi}{\partial \lambda_{b,1}} = 0, \quad \frac{\partial \Pi}{\partial \bar{h}} = 0, \quad (\text{S36})$$

where

$$\frac{\partial \Pi}{\partial \lambda_{a,1}} = \frac{1}{2}D\bar{h}L^2\mu \left(2\lambda_{a,1} - \frac{2}{\lambda_{a,1}^3\lambda_{a,3}^2} \right) - \bar{h}LF \left(1 - \frac{1}{\lambda_{a,1}^2\lambda_{a,3}} \right), \quad (\text{S37})$$

$$\begin{aligned} \frac{\partial \Pi}{\partial \lambda_{a,3}} = & \frac{1}{2}D\bar{h}L^2\mu \left(2\lambda_{a,3} - \frac{2}{\lambda_{a,1}^2\lambda_{a,3}^3} \right) + \frac{1}{2}D(1 - \bar{h})L^2\mu \left(\frac{2(1 - \bar{h})^2\bar{h}}{\lambda_{b,1}^2(1 - \bar{h}\lambda_{a,3})^3} - \frac{2\bar{h}(1 - \bar{h}\lambda_{a,3})}{(1 - \bar{h})^2} \right) \\ & + \frac{\bar{h}LF}{\lambda_{a,1}\lambda_{a,3}^2} - \frac{\bar{h}(1 - \bar{h})^2LF}{\lambda_{b,1}(1 - \bar{h}\lambda_{a,3})^2}, \end{aligned} \quad (\text{S38})$$

$$\frac{\partial \Pi}{\partial \lambda_{b,1}} = \frac{1}{2}D(1 - \bar{h})L^2\mu \left(2\lambda_{b,1} - \frac{2(1 - \bar{h})^2}{\lambda_{b,1}^3(1 - \bar{h}\lambda_{a,3})^2} \right) - (1 - \bar{h})LF \left(1 - \frac{1 - \bar{h}}{\lambda_{b,1}^2(1 - \bar{h}\lambda_{a,3})} \right), \quad (\text{S39})$$

$$\begin{aligned} \frac{\partial \Pi}{\partial \bar{h}} = & -\frac{1}{2}DL^2\mu \left(\frac{(1 - \bar{h})^2}{\lambda_{b,1}^2(1 - \bar{h}\lambda_{a,3})^2} + \frac{(1 - \bar{h}\lambda_{a,3})^2}{(1 - \bar{h})^2} + \lambda_{b,1}^2 - 3 \right) \\ & + \frac{1}{2}D(1 - \bar{h})L^2\mu \left(\frac{2(1 - \bar{h})^2\lambda_{a,3}}{\lambda_{b,1}^2(1 - \bar{h}\lambda_{a,3})^3} - \frac{2(1 - \bar{h})}{\lambda_{b,1}^2(1 - \bar{h}\lambda_{a,3})^2} + \frac{2(1 - \bar{h}\lambda_{a,3})^2}{(1 - \bar{h})^3} - \frac{2\lambda_{a,3}(1 - \bar{h}\lambda_{a,3})}{(1 - \bar{h})^2} \right) \\ & + \frac{1}{2}DL^2\mu \left(\frac{1}{\lambda_{a,1}^2\lambda_{a,3}^2} + \lambda_{a,1}^2 + \lambda_{a,3}^2 - 3 \right) + LF \left(\frac{1 - \bar{h}}{\lambda_{b,1}(1 - \bar{h}\lambda_{a,3})} + \lambda_{b,1} - 2 \right) \\ & - (1 - \bar{h})LF \left(\frac{(1 - \bar{h})\lambda_{a,3}}{\lambda_{b,1}(1 - \bar{h}\lambda_{a,3})^2} - \frac{1}{\lambda_{b,1}(1 - \bar{h}\lambda_{a,3})} \right) - LF \left(\frac{1}{\lambda_{a,1}\lambda_{a,3}} + \lambda_{a,1} - 2 \right). \end{aligned} \quad (\text{S40})$$

Since we could not solve Eq. (S36) analytically, we used the *fmincon* function in Matlab (Mathworks) to find the lowest energy states. More specifically, we started from the undeformed configuration for which $F = 0$ and $\lambda_{a,i} = \lambda_{b,i} = 1$ ($i = 1, 2, 3$) and set $\bar{h} = 0.5$. We then incrementally increased F by $\Delta F = \mu LD/100$ to find the

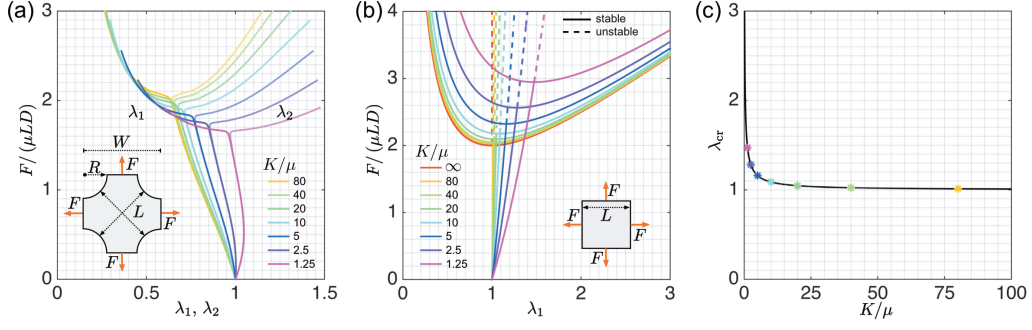


FIG. S2: Effect of material compressibility. (a) Relation between the applied force F and the stretches of the diagonals λ_1 and λ_2 as a function of K/μ for a cross-shape sample under plane strain conditions subjected to equibiaxial tension. (b) Relation between the applied force F and the stretches of the diagonals λ_1 and λ_2 as a function of K/μ for a square under plane strain conditions subjected to equibiaxial tension. (c) Evolution of the critical stretch as a function of K/μ for a square under plane strain conditions subjected to equibiaxial tension.

equilibrium path (note that we used $\Delta F = \mu LD/10000$ around the instability). The minimal energy path predicted by our numerical calculations is shown in Fig. S1(a). Upon loading, the system does not deform until $F/(\mu LD) = 2$ as shown in Fig. S1(b), and as such the internal energy U of the block remains zero. However, at $F/(\mu LD) = 2$ a snap-through instability occurs instantly lowering the potential energy Π (see inset in Fig. S1(a)). Interestingly, for $F/(\mu LD) > 2$ both layers flatten and deform into two flat plates rotated 90 degrees with respect to each other. Moreover, we find that for $F/(\mu LD) > 2$, $\lambda_{a,1} = \lambda_{a,3} = \lambda_{b,1}$ as shown in Fig. S1(b).

Next, guided by our numerical results, we turn back to Eqs. (S35)-(S40) and assume that $\lambda_{a,3} = \lambda_{a,1}$, and $\lambda_{b,1} = \lambda_{a,1}$. The terms from Eqs. (S37)-(S40) then simplify, such that

$$\frac{\partial \Pi}{\partial \lambda_{a,1}} = \mu L^2 D \bar{h} \left(\lambda_{a,1} - \frac{1}{\lambda_{a,1}^5} \right) - FL \bar{h} \left(1 - \frac{1}{\lambda_{a,1}^3} \right) = 0, \quad (S41)$$

$$\frac{\partial \Pi}{\partial \lambda_{b,1}} = \mu L^2 D (1 - \bar{h}) \left(\lambda_{a,1} - \frac{(1 - \bar{h})^2}{\lambda_{a,1}^3 (1 - \bar{h} \lambda_{a,1})^2} \right) - FL (1 - \bar{h}) \left(1 - \frac{1 - \bar{h}}{\lambda_{a,1}^2 (1 - \bar{h} \lambda_{a,1})} \right) = 0, \quad (S42)$$

while $\partial \Pi / \partial \lambda_{a,3} = 0$ and $\partial \Pi / \partial \bar{h} = 0$ are automatically satisfied when Eqs. (S41)-(S42) are satisfied. Interestingly, there are two distinct solutions to Eqs. (S41)-(S42)

$$\lambda_{a,1} = 1 \quad \text{with} \quad 0 \leq \bar{h} \leq 1, \quad (S43)$$

$$\frac{F}{\mu LD} = \lambda_{a,1} + \frac{1}{\lambda_{a,1}^2} \quad \text{with} \quad \bar{h} = \frac{\lambda_{a,1}^2 - 1}{\lambda_{a,1}^3 - 1}. \quad (S44)$$

Finally, by combining Eqs. (S23)-(S24) and (S43)-(S44), all the stretches in the two layers can be determined

$$\lambda_{a,3} = \lambda_{b,1} = \lambda_{b,2} = \lambda_{a,1}, \quad (S45)$$

$$\lambda_{a,2} = \lambda_{b,3} = \lambda_{a,1}^{-2}. \quad (S46)$$

Importantly, we find that the solutions defined by Eqs. (S43)-(S44) are identical to those found for a cube subjected to equitriaxial tension (Eqs. (S7)-(S8)), and that a bifurcation occurs at $F/(\mu LD) = 2$. For $F/(\mu LD) < 2$ the system does not deform (as illustrated in Fig. 3(e) for $F/(\mu LD) = 3/2$), while for $F/(\mu LD) > 2$ one of the layer extends and the other flattens in the out-of-plane direction (as illustrated in Fig. 3(e) for $F/(\mu LD) = 5/2$), resulting in a wavy pattern that closely resembles the deformation shown in Figs. 2(b) and 3(a).

EFFECT OF MATERIAL COMPRESSIBILITY

In our simulations, the choice of $K/\mu = 20$ (resulting in a Poisson's ratio of 0.475) was dictated by numerical considerations. Note that the stable time increment for our 3D explicit analyses is given by

$$\Delta t = \frac{L}{c}, \quad (S47)$$

where L is a characteristic length of the elements and c is the wave speed in a 3D-medium,

$$c = \sqrt{\frac{E(1-\nu)}{\rho(1+\nu)(1-2\nu)}}, \quad (\text{S48})$$

ν being the Poisson's ratio. From Equation (S48) it becomes clear that when the materials approaches incompressibility (i.e $\nu \rightarrow 1/2$ and $K/\mu \rightarrow \infty$), Δt becomes very small, resulting in significantly longer simulation time (note that Abaqus only allows for $K/\mu \leq 100$, corresponding to a Poisson's ratio of $\nu = 0.495$). To find a compromise between simulation time and accuracy (as we wanted to preserve a nearly incompressible behavior in our analysis), we simulated the response of a cross-shaped sample under plane strain conditions subjected to equibiaxial tension for different values of K/μ . First, the results reported in Fig. S2(a) indicate that the instability is triggered for all the considered values of K/μ . However, as K/μ decreases, smaller forces are needed to trigger the bifurcation. Second, we find that the response of the sample characterized by $K/\mu = 20$ and $K/\mu = 80$ are very close to each other, so we choose $K/\mu = 20$ as it provides a good balance between accuracy and simulation speed.

Note that we can also study analytically the effect of the ratio K/μ by determining the response of a compressible square under plane strain conditions. To this end, we use the strain energy of a nearly incompressible Neo Hookean material [1, 7]

$$W = \frac{\mu}{2} (\lambda_1^2 + \lambda_2^2 + \lambda_3^2 - 3) + \frac{K}{2} (\lambda_1 \lambda_2 \lambda_3 - 1)^2 - \mu \log(\lambda_1 \lambda_2 \lambda_3). \quad (\text{S49})$$

The total energy for the square under biaxial tension is then given by

$$\Pi = \frac{\mu L^2 D}{2} (\lambda_1^2 + \lambda_2^2 - 2) + \frac{K L^2 D}{2} (\lambda_1 \lambda_2 - 1)^2 - \mu L^2 D \log(\lambda_1 \lambda_2) - FL(\lambda_1 + \lambda_2 - 2), \quad (\text{S50})$$

where we have used the fact that $\lambda_3 = 1$ due to plane strain conditions. The equilibrium solutions are found by minimizing Π with respect to λ_1 and λ_2 ,

$$\frac{\partial \Pi}{\partial \lambda_1} = \mu L^2 D \lambda_1 + K L^2 D (\lambda_1 \lambda_2 - 1) \lambda_2 - \frac{\mu L^2 D}{\lambda_1} - FL = 0, \quad (\text{S51})$$

$$\frac{\partial \Pi}{\partial \lambda_2} = \mu L^2 D \lambda_2 + K L^2 D (\lambda_1 \lambda_2 - 1) \lambda_1 - \frac{\mu L^2 D}{\lambda_2} - FL = 0, \quad (\text{S52})$$

which are only satisfied when

$$\frac{F}{\mu L D} = \frac{(\lambda_1^2 - 1) \left(\frac{K}{\mu} \lambda_1^2 + 1 \right)}{\lambda_1} \quad \text{with} \quad \lambda_2 = \lambda_1, \quad (\text{S53})$$

or

$$\frac{F}{\mu L D} = \frac{\sqrt{\frac{K^2}{\mu^2} + 6 \frac{K}{\mu} + 1} + 2 \frac{K}{\mu} \lambda_1^2 + \frac{K}{\mu} + 1}{2 \frac{K}{\mu} \lambda_1} \quad \text{with} \quad \lambda_2 = \frac{\sqrt{\frac{K^2}{\mu^2} + 6 \frac{K}{\mu} + 1} + \frac{K}{\mu} + 1}{2 \frac{K}{\mu} \lambda_1}. \quad (\text{S54})$$

These two equilibrium solutions are shown in Figure S2(b) for various ratios of K/μ . Similarly to the numerical results reported in Figure S2(a) for the cross-shaped sample, the analysis indicates that the instability still occurs even if the material is compressible. Moreover, by comparing Equations (S53) and (S54) we can determine the stretch, λ_{cr} , at which the solutions become unstable

$$\lambda_{\text{cr}} = \sqrt{\frac{1}{2} + \sqrt{\frac{\mu^2}{4K^2} \left(2 + 6 \frac{K}{\mu} + \frac{K^2}{\mu^2} + 2 \sqrt{1 + 6 \frac{K}{\mu} + \frac{K^2}{\mu^2}} \right)}}, \quad (\text{S55})$$

In Figure S2(c) we report the evolution of λ_{cr} as a function of K/μ . The results clearly indicate that the critical stretch for $K/\mu = 20$ is very close to that found for the incompressible case.

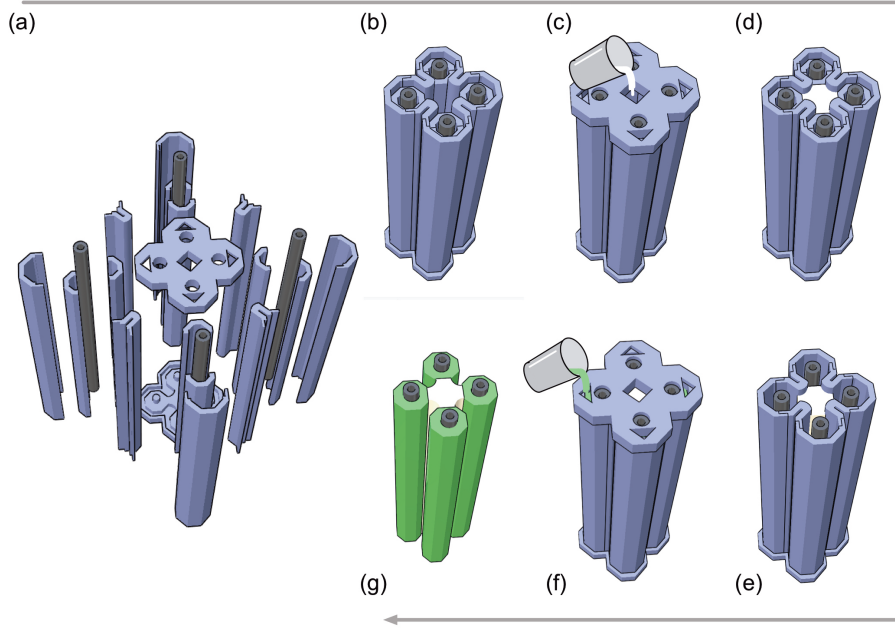


FIG. S3: Fabrication of the sample. (a) The 3D printed mold and the steel tubes prior to assembly. (b) Assembled mold. (c) Casting of the Ecoflex 0030. (d)-(e) After two hours some inner parts are removed to make room for the second casting step. (f) Casting of the Elite Double 32. (g) After approximately one day, the sample is fully cured and can be removed from the mold.

EXPERIMENTS

Fabrication

The samples were fabricated using a molding process (Fig. S3)). To cast a multi-material sample, and to allow for easy removal after curing, the mold was assembled from several 3D printed parts (Stratasys Connex500) and steel tubes (Fig. S3(a)). Casting the sample consisted of several steps. We first assembled the mold as shown in Fig. S3(b). Second, a silicone-based rubber Ecoflex 0030 (Smooth-On, Inc.) was cast in the center of the mold as shown in Fig. S3(c). Before casting, we degassed the Ecoflex for 1 minute to remove any air bubbles still present after mixing of the two components. After letting the Ecoflex cure for 2 hours at room temperature, part of the mold was removed to prepare for the second casting step (Figs. S3(d)-(e)). Next, another silicone-based rubber Elite Double 32 (Zhermack) was cast around the four metal tubes already present in the mold (Fig. S3(f)). Note that at this point the Ecoflex was not yet fully cured, but was able to support itself. This improved the bonding between the Ecoflex 0030 and the Elite Double 32 in the final samples. We tested different curing durations, but found that curing the Ecoflex for 2 hours in the first step provided the best bonding. Finally, the sample was removed from the mold after approximately 1 day (Fig. S3(g)).

The cured Ecoflex 0030 was tested under uniaxial tension using a single-axis Instron (model 5544A; Instron, Inc.) with a 1000-N load cell. The material behavior up to a stretch of 300% is reported in Fig. S4. We used a least squares method to fit an incompressible Neo-Hookean model (Eq. (S1)) to the measured data, and found that the material response is best capture with an initial shear modulus $\mu = 0.0216$ MPa.

Testing

The samples were stretched equibiaxially using a custom made setup consisting of an aluminium frame to which the sample was connected by four steel cables (Fig. S5). Four screws were manually tightened to stretch the sample. Since boundary effects prevented us to clearly observe the instability upon stretching (Movie 1), we acquired x-ray transmission images (HMXST225, X-Tek) after each time we turned the screws a full turn. Note that a full turn of the screws results in an applied displacement $u/W = 0.18$. The results are shown in Fig. 2 and Movie 1.

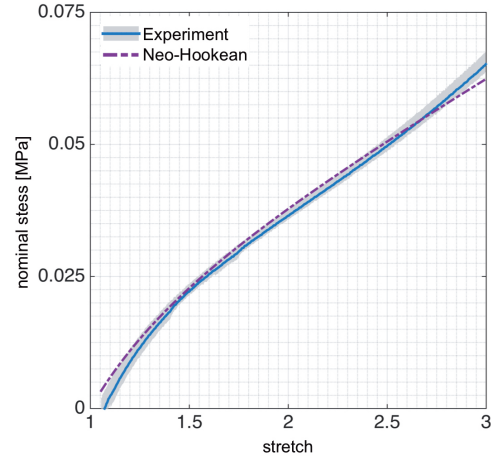


FIG. S4: Nominal stress versus stretch for the cured Ecoflex 0030 obtained from a uniaxial tension test. The experiments were fitted using a Neo-Hookean material model with initial shear modulus $\mu = 0.0216$ MPa.

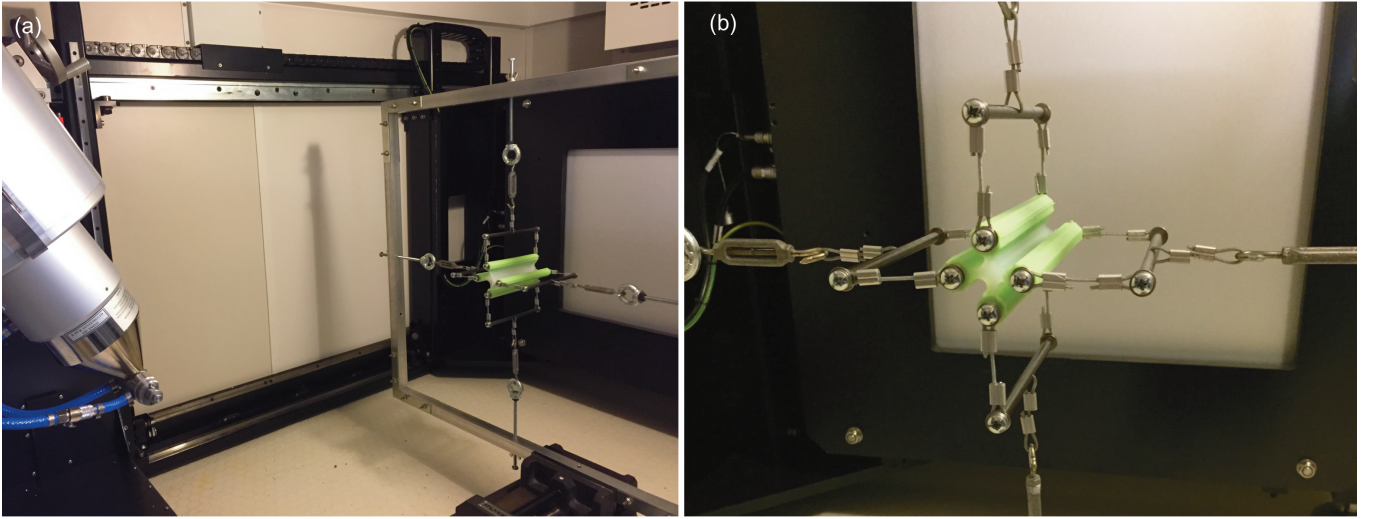


FIG. S5: (a) Test-setup used to biaxially stretch the sample. (b) Close-up view of the undeformed sample suspended in the test-setup.

ADDITIONAL FIGURES

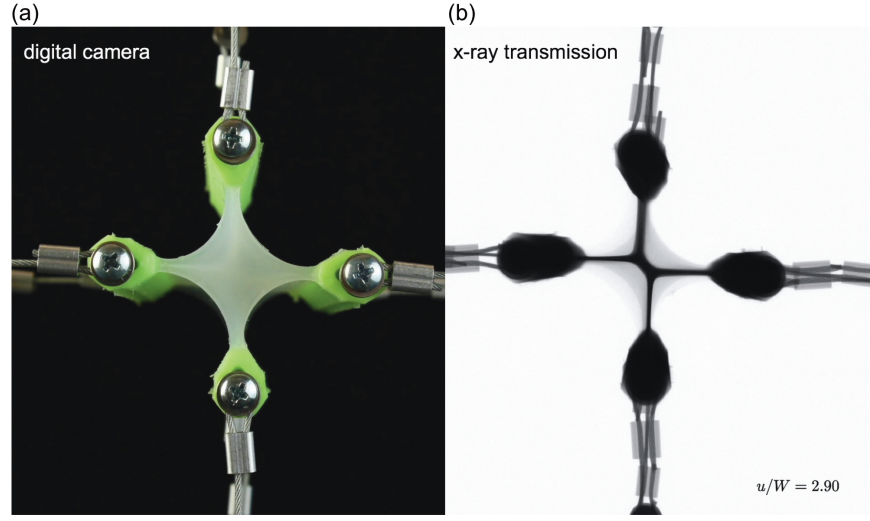


FIG. S6: (a) Front view of the sample at $u/W = 2.90$ obtained using a digital camera (D90 SLR, Nikon). (b) Cross-sectional view of the sample at $u/W = 2.90$ obtained using a micro-CT X-ray imaging machine (HMXST225, X-Tek).

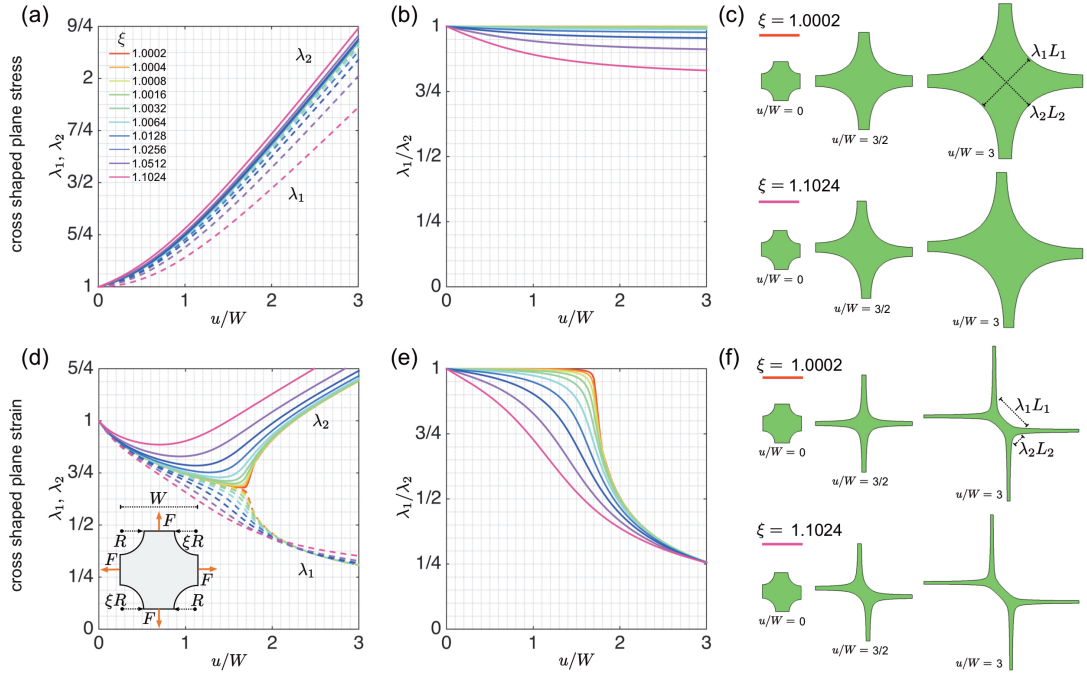


FIG. S7: 2D finite element simulations highlighting the effect of imperfections. Each simulation consists of a square with edges of length W and circles of radius $R_1 = 0.31W$ and $R_2 = \xi 0.31W = \xi R_1$ cut from its opposite corners, so that the two diagonals located at the center of the sample are given by $L_1 = \sqrt{2}W - 2R$ and $L_2 = \sqrt{2}W - 2\xi R$. An outward displacement is applied to the straight boundaries of the sample, and we monitored the evolution of the two diagonals with length $\lambda_1 L_1$ and $\lambda_2 L_2$ in the stretched configuration. The simulations are performed assuming both plane stress (a-c) and plane strain (d-f) conditions.

-
- [1] R. Ogden, *Non-Linear Elastic Deformations* (Dover New York, 1988).
 - [2] R. S. Rivlin, Philosophical Transactions of the Royal Society of London A: Mathematical, Physical and Engineering Sciences **240**, 491 (1948).
 - [3] R. Hill, Journal of the Mechanics and Physics of Solids **5**, 229 (1957).
 - [4] M. F. Beatty, International Journal of Solids and Structures **3**, 23 (1967).
 - [5] R. S. Rivlin, *Collected Papers of R.S. Rivlin: Volume I and II* (Springer New York, New York, NY, 1997), chap. Stability of Pure Homogeneous Deformations of an Elastic Cube under Dead Loading, pp. 398–404.
 - [6] J. M. Ball and D. G. Schaeffer, Mathematical Proceedings of the Cambridge Philosophical Society **94**, 315 (1983).
 - [7] M. C. Boyce and E. M. Arruda, Rubber Chemistry and Technology **73**, 504 (2000).